ELSEVIER

Composite Structures 55 (2002) 63–71

COMPOSITE STRUCTURES

www.elsevier.com/locate/compstruct

Analysis of filament wound composite structures considering the change of winding angles through the thickness direction

Jae-Sung Park, Chang-Sun Hong *, Chun-Gon Kim, Cheol-Ung Kim

Department of Mechanical Engineering, Division of Aerospace Engineering, Korea Advanced Institute of Science and Technology, 373-1 Kusong-Dong, Yusong-Ku, Taejon 305-701, Republic of Korea

Abstract

In this study, filament winding patterns were calculated using a semi-geodesic fiber path equation for an arbitrary surface. Because the fiber path depends on the surface where fibers are wound, the winding angle varies in the longitudinal and thickness directions of a wound structure. The fiber angle difference through the thickness was calculated for several design parameters, such as helical winding thickness and angle. Finite element analyses were performed considering the change of winding angles through the thickness by a commercial FEA code, ABAQUS. A user subroutine, ORIENT, was coded to impose the change of winding angles to each solid element. Water-pressuring tests were performed for an advanced standard test evaluation bottle (ASTEB). The results of the finite element analysis considering geometrical nonlinearities were verified with the experimental data.

Keywords: Filament winding; Semi-geodesic path equation; ABAQUS

1. Introduction

The high specific strength and stiffness of advanced composite materials often make these materials attractive candidates for weight sensitive structures, especially rockets and missiles. The axial-symmetric structure like a pressure tank or a motor case in the rocket structure would be made out of composite materials usually using filament winding process. In spite of their good performance, pressure tanks made by filament winding have complexity in analyzing the geometry and properties in their dome parts along the longitudinal axis. As the wound layers are added on a cylindrical mandrel, the curvilinear fiber path leads to a continuous change in the winding angle and thickness. In addition, the fiber angle varies in the thickness direction because the fiber path depends on the surface on which fibers are wound. Therefore finite element analyses, which can handle the winding angle and thickness variation, are required to predict the exact behavior of pressure tanks.

Isotensoid dome design [1], modified helically wound dome design [2] and planar wound dome design method [3] have been used to determine the winding patterns and dome geometry of pressure vessels. An isotensoid vessel is assumed to support internal pressure by the fiber only and to consist of filaments that are loaded to an identical stress level. It is mainly used, when both openings of a pressure vessel have the same radius. Planar fiber patterns lie in a plane, which is tangent to the polar opening at one end of the part and tangent to the opposite side of the polar opening at the other end. these are mainly used in pressure vessels with length-to-diameter ratios of <1.8. Because these previous methods calculated the dome shape and winding pattern simultaneously, initially determined winding patterns were maintained till the end of the winding process. Recently many researchers have the calculated possible winding patterns considering fiber slip which occurs at the dome region during the winding process. These studies make it possible to manufacture even the nonaxial-symmetric structures using filament winding [4,5]. However, no literature considered the change of winding angle through the thickness direction in the analysis of filament wound pressure vessels. The fiber path depends on the surface where the fibers are wound and the shape of the surface is changing with already built-up fibers as the filament winding process is carried out. Especially the surface change during the winding process becomes relatively large because the thickness is thicker near the polar opening than in the other dome parts, so it should

* Corresponding author. Tel.: +82-42-869-3712; fax: +82-42-869-3710.

E-mail address: cshong@cais.kaist.ac.kr (C.-S. Hong).

0263-8223/01/$ - see front matter
PII: S0263-8223(01)00137-4

not be ignored. Therefore the fiber angle must be recalculated in the thickness direction to consider the changed shape of the dome surface during the winding process even at the same axial position of the dome region.

In most of the finite element analyses of filament wound pressure tanks, shell and axial-symmetric solid elements have been used [2,6,7]. For an axial-symmetric solid element, three-dimensional effective moduli are needed and layerwise stress and strain components are not available unless each layer is modeled, respectively. When shell elements are adopted in the analysis, the detailed modeling of a metallic boss bonded to the composite is not easy and the critical failure modes such as a boss blow-out in the wound motor case cannot be predicted. The dome/polar boss interface is one of the most highly stressed areas of a filament wound composite motor case, because all the internal pressure acting across the polar openings must be transferred to the composite in this area. In addition, the stress concentration at cylinder/dome junction region is sometimes overestimated due to the rapid change in thickness and curvature of shell elements unless enough elements are used in the dome/cylinder interface region.

In the present study, the fiber angle distribution at the dome was calculated for arbitrary mandrel surfaces using a semi-geodesic path equation. Geodesic lines connect two points along the shortest distance over the surface. In this case no friction force is required to keep the fiber from slipping, since it follows a self-stable trajectory. The semi-geodesic path is slightly deviating from the geodesic path counting on friction to keep the fiber in its proper position. In addition, the fiber winding angle change through the thickness during the winding process was quantified for various design parameters, such as winding thickness and helical winding angle. Geometrically nonlinear finite element analyses considering the change of winding angles through the thickness were performed. Water-pressuring tests were done for ASTEB to verify FE analyses by comparing the strain distribution measured over the dome region with the calculated results. The effect of several stiffening methods using dome-caps and wafers was investigated on the mechanical behavior of the composite pressure vessels.

2. Calculation of filament winding patterns

2.1. Semi-geodesic path equation

The geometry and winding patterns are the basic parameters to manufacture a filament wound structure. Previous methods to design the dome geometry were based on the stable winding patterns, called geodesic patterns. The geodesic path is a curve connecting two points on a surface according to the shortest distance over this surface. So a fiber placed along a geodesic line will not tend to slip when being pulled. Hence, geodesic winding does not require any friction to be stable. However, geometry and winding patterns were calculated simultaneously in the geodesic winding, so that the mandrel shape was determined beforehand from the winding angle and radius ratio between the opening and cylindrical parts. Sometimes it is required to calculate the winding patterns for pre-designed dome shapes, such as hemispherical domes or manufactured liners. In order to calculate the winding patterns for an arbitrary surface, the semi-geodesic fiber path equation is induced for an arbitrary surface of revolution in the present study. Slippage tendency (λ) which represents the frictional force between the wet tow and the mandrel was introduced to find the region of possible winding patterns. The friction coefficient between a mandrel and fiber ranges from 0.2 (wet winding) to 0.39 (dry winding) [5].

A detailed derivation of the equations can be found in [4].

An arbitrary surface of revolution about the x-axis is defined as $\vec{S}(x,\theta)$ with x, the axial coordinate and θ, the circumferential coordinate in Fig. 1. The fiber follows a path

$$\vec{\Gamma}(s) = [\,x(s) \quad \theta(s)\,]^{\mathrm{T}}$$

on the surface $\vec{S}(x,\theta)$

$$\vec{S}(x,\theta) = [\,x \quad r(x)\cos\theta \quad r(x)\sin\theta\,]^{\mathrm{T}}. \tag{1}$$

The normalized basis vectors of the surface in the x and θ directions are:

$$\vec{S}_x = \left[\frac{1}{A} \quad \frac{r'}{A}\cos\theta \quad \frac{r'}{A}\sin\theta\right]^{\mathrm{T}}, \tag{2}$$

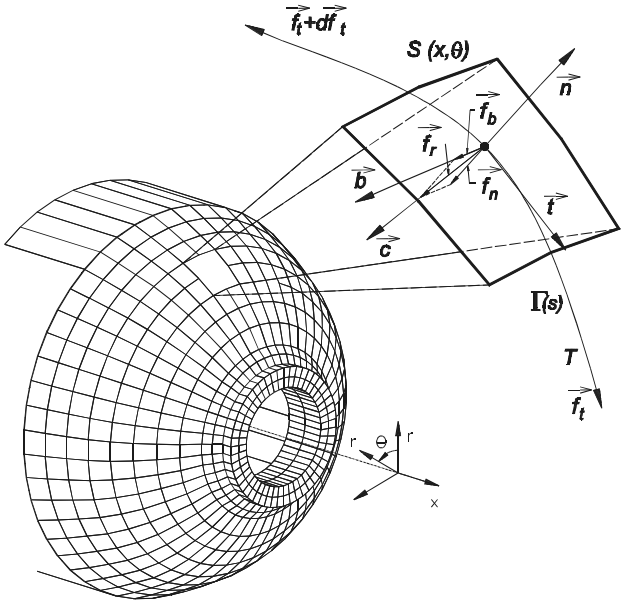

Fig. 1. Geometry of fiber path on surface $S(x,\theta)$.

$$\vec{S}_\theta = [\,0 \quad -\sin\theta \quad \cos\theta\,]^{\mathrm{T}} \tag{3}$$

with $r' = \mathrm{d}r/\mathrm{d}x$ and $A = \sqrt{1+r'^2}$.

There are two ways to calculate the tangent vector, $\vec{t}$, to the fiber path. One can be written as the derivatives of Eq. (1)

$$\vec{t} = \frac{\mathrm{d}\vec{S}}{\mathrm{d}s} = \left[\,\frac{\mathrm{d}x}{\mathrm{d}s} \quad r'\frac{\mathrm{d}x}{\mathrm{d}s}\cos\theta - r\frac{\mathrm{d}\theta}{\mathrm{d}s}\sin\theta \quad r'\frac{\mathrm{d}x}{\mathrm{d}s}\sin\theta + r\frac{\mathrm{d}\theta}{\mathrm{d}s}\cos\theta\,\right]^{\mathrm{T}}. \tag{4}$$

Another can be written with the normalized basis vectors and winding angle, α, i.e., the angle between the tangent to the fiber path and the generatrix of the surface of revolution, measured in the tangent plane to the surface

$$\vec{t} = \vec{S}_x\cos\alpha + \vec{S}_\theta\sin\alpha = \frac{1}{A}\begin{bmatrix}\cos\alpha \\ r'\cos\theta\cos\alpha - A\sin\theta\sin\alpha \\ r'\sin\theta\cos\alpha + A\cos\theta\sin\alpha\end{bmatrix}. \tag{5}$$

By comparing Eqs. (4) and (5), the relation between $\mathrm{d}\theta/\mathrm{d}s$, $\mathrm{d}x/\mathrm{d}s$ and the winding angle, α, can be derived:

$$\frac{\mathrm{d}\theta}{\mathrm{d}s} = \frac{\sin\alpha}{r}, \tag{6}$$

$$\frac{\mathrm{d}x}{\mathrm{d}s} = A\cos\alpha = \frac{\cos\alpha}{\sqrt{1+r'^2}}. \tag{7}$$

The fiber tension $\vec{f}_{\mathrm{t}}$ leads to a force $\vec{f}_{\mathrm{r}} = \mathrm{d}\vec{f}_{\mathrm{t}}/\mathrm{d}s$ per unit length on the mandrel surface, which is directed towards the center of curvature of the fiber path. The resultant force $\vec{f}_{\mathrm{r}}$ can be split into two components: the normal force $\vec{f}_{\mathrm{n}}$, perpendicular to the surface and the transverse force $\vec{f}_{\mathrm{b}}$, tangential to the mandrel surface. Then the slippage tendency, λ, is defined as the ratio between the transverse force, $\vec{f}_{\mathrm{b}}$, and the normal force, $\vec{f}_{\mathrm{n}}$

$$\lambda = \frac{\|\vec{f}_{\mathrm{b}}\|}{\|\vec{f}_{\mathrm{n}}\|} = \frac{\vec{f}_{\mathrm{r}}\cdot\vec{b}}{\vec{f}_{\mathrm{r}}\cdot\vec{n}} = \frac{\vec{c}\cdot\vec{b}}{-\vec{c}\cdot\vec{n}}, \tag{8}$$

where $\vec{c}$ is the curvature vector, $\vec{n}$ is the normal vector of the surface and $\vec{b}$ is the binormal vector.

The curvature vector is directed towards the center of curvature of the curve and equals

$$\vec{c} = \frac{\mathrm{d}t}{\mathrm{d}s} = \vec{S}_x\frac{\mathrm{d}^2x}{\mathrm{d}s^2} + \vec{S}_\theta\frac{\mathrm{d}^2\theta}{\mathrm{d}s^2} + \vec{S}_{xx}\left(\frac{\mathrm{d}x}{\mathrm{d}s}\right)^2 + 2\vec{S}_{x\theta}\frac{\mathrm{d}x}{\mathrm{d}s}\frac{\mathrm{d}\theta}{\mathrm{d}s} + \vec{S}_{\theta\theta}\left(\frac{\mathrm{d}\theta}{\mathrm{d}s}\right)^2. \tag{9}$$

The normal, $\vec{n} = -\vec{S}_x\times\vec{S}_\theta$, on the surface equals

$$\vec{n} = \left[\,\frac{-r'}{A} \quad \frac{1}{A}\cos\theta \quad \frac{1}{A}\sin\theta\,\right]^{\mathrm{T}}. \tag{10}$$

The binormal, $\vec{b}$, can be calculated as follows:

$$\vec{b} = \vec{t}\times\vec{n} = \frac{1}{A}\begin{bmatrix}-\sin\alpha \\ -A\sin\theta\cos\alpha + r'\cos\theta\sin\alpha \\ -r'\sin\theta\sin\alpha - A\cos\theta\cos\alpha\end{bmatrix}. \tag{11}$$

Eq. (8) can be simplified as Eq. (12) with Eqs. (9)–(11)

$$\lambda = \frac{A^2r'\sin\alpha + A^3r(\mathrm{d}\alpha/\mathrm{d}s)}{A^2\sin^2\alpha - rr''\cos^2\alpha} \tag{12}$$

or as a function of $\mathrm{d}\alpha/\mathrm{d}s$

$$\frac{\mathrm{d}\alpha}{\mathrm{d}s} = \frac{\lambda\left(A^2\sin^2\alpha - rr''\cos^2\alpha\right) - A^2r'\sin\alpha}{A^3r}. \tag{13}$$

Multiplying Eq. (7) by Eq. (13) yields Eq. (14).

$$\frac{\mathrm{d}\alpha}{\mathrm{d}x} = \frac{\lambda(A^2\sin^2\alpha - rr''\cos^2\alpha) - r'A^2\sin\alpha}{rA^2\cos\alpha}. \tag{14}$$

By integrating Eq. (14) from the known winding angle, $\alpha = 90°$, at the end of the dome, the winding angle, α, can be calculated for the entire dome surface. Two assumptions are underlying in the calculation of the thickness in the dome part: fiber volume fraction is maintained consistently and the number of fibers in a cross-section is always constant. With these assumptions, the thickness along the longitudinal direction can be derived as follows:

$$(2\pi r)t\cos\alpha = (2\pi r_{\mathrm{c}})t_{\mathrm{c}}\cos\alpha_{\mathrm{c}}, \tag{15}$$

$$t = \frac{r_{\mathrm{c}}\cos\alpha_{\mathrm{c}}}{r\cos\alpha}\times t_{\mathrm{c}}, \tag{16}$$

where r_{c}, α_{c}, t_{c} are the radius, fiber angle and thickness of the cylindrical region.

As the winding fiber approaches the opening, winding angle (α) becomes 90° and the right-hand side of Eq. (16) becomes infinity, and so does the thickness theoretically. Thickness divergence is caused by fiber concentration on a relatively small area. That is to say, the fiber rotates repetitively around the polar boss in numerical calculation before it winds to the opposite direction. Thus the winding thickness is corrected to be constant from 98% to 100% of the meridian length measured from the cylinder–dome junction in this study.

2.2. Fiber angle change through the thickness direction

As mentioned in Section 1, the winding angle changes through the thickness direction at the dome part for a fixed helical winding angle. The mechanical behavior of the wound part can be derived from the theoretical data of fiber alignment and thickness distribution. But if accurate winding angle distributions are not considered, the behavior of the wound part cannot be predicted precisely. Therefore it is required to determine the angle variation in the thickness direction. The fiber path and

thickness of the first ply were calculated beforehand from the given mandrel shape. The second ply was wound on the top surface of the first ply. From the summed thickness of previous plies, the fiber path and thickness of the next ply could be generated up to the given number of plies. The steps for considering the winding angle change are shown in Fig. 2.

The difference in fiber angles between the first and last plies was predicted for several design parameters, such as winding thickness and helical winding angle. Difference of winding angles is calculated for an EXOS-B model, which was designed by the isotensoid dome design method and was used as a motor case for a scientific satellite in Japan [1]. The wall thickness of EXOS-B is originally 2.3 mm but changed from 3.03 to 3.86 mm with respect to the thickness ratio of the STEB and the ASTEB. The STEB is fundamentally a one-ninth scale of a typical second-stage motor case and is intended to be a standard for comparing materials, processes, and design features [8]. The ASTEB is also developed to evaluate the performance of small scaled pressure vessels with respect to the design and processing parameters. It is a modified version of the STEB and has a bigger opening radius than the STEB. Table 1 shows the configuration of each bottle.

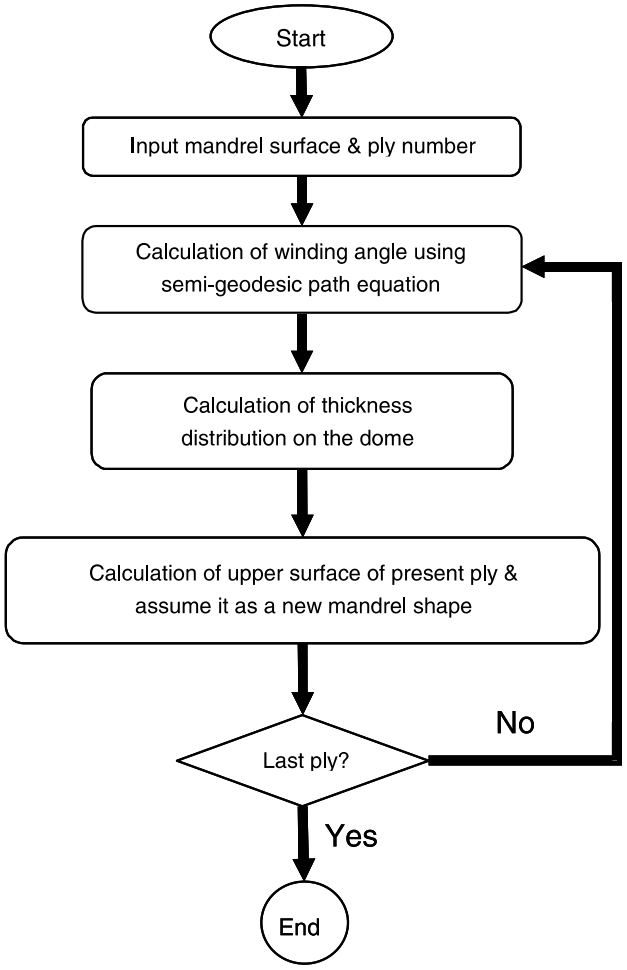

Fig. 2. Calculation algorithm to consider the angle variation through the thickness.

Table 1
Configuration of various bottles

		Forward dome (mm)	Aft dome (mm)
EXOS-B	Cylinder radius, R_c	350.0	350.0
	Boss radius, R_b	148.1	–
	Cylinder thickness, t_c	2.3	2.3
	Hoop winding thickness, t_h	2.4	2.4
STEB	Cylinder radius, R_c	127.0	127.0
	Boss radius, R_b	22.05	47.70
	Cylinder thickness, t_c	1.4	1.4
	Hoop winding thickness, t_h	1.6	1.6
ASTEB	Cylinder radius, R_c	127.0	127.0
	Boss radius, R_b	45.80	70.83
	Cylinder thickness, t_c	1.0	1.0
	Hoop winding thickness, t_h	1.113	1.113

3. Finite element analysis and experiment

3.1. Finite element modeling

The finite element analyses considering the geometrical nonlinearity were performed for the ASTEB. The original mesh and boundary conditions used in this finite element analysis are shown in Fig. 3. 1.5° strip of the full ASTEB was modeled using a cyclic symmetric condition at both sides. The forward and aft domes are analyzed separately, because stress remains constant shortly away from the dome/cylinder interface. The three-dimensional solid elements (C3D27R) with

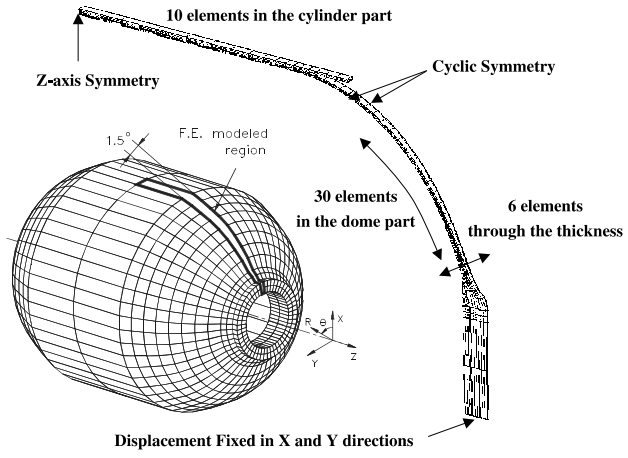

Fig. 3. Finite element mesh used in the analysis.

reduced integration in ABAQUS are selected for a composite and metallic boss. This strip was meshed into 30 elements in the meridian direction of each dome part and one element per each layer in the thickness direction. Six elements are applied in the thickness direction to model three $\pm 27^\circ$ layers. Between the solid boss and the composite winding, the gasket elements (GK3D18) are located to simulate a rubber layer. By using this rubber layer, slip between the composite dome and metallic boss could be modeled. Because the stress becomes constant along the longitudinal direction in the cylindrical part, only a small portion of the cylinder was included in the analysis even though the cylindrical part is almost twice longer than the dome length. Internal pressure was applied up to 6.23 MPa at the inner surface of solid elements.

The winding angle for each element at the dome region was pre-calculated using the semi-geodesic path equation with the given helical winding angle of $\pm 27^\circ$. Then the user subroutine, ORIENT, reads the angle data at each integration point of elements and transforms the local coordinates calculated from the position of nodes to the fiber directions. The fiber angle does not change rapidly at the cylinderical region and most of the dome region, but varies abruptly at the end of the dome. Therefore it is required to use enough number of elements and to consider the gradient in the fiber angle for each element as precise as possible near the opening. The size of the element is bigger at the center of the dome than near the interface of the dome/cylinder and dome/polar opening. 20 elements are enough to gain a converged result, but 30 elements are used in the dome area. The change of the winding angle during the winding process was quantified by the layer-wise calculation of the winding angle.

Because the regions near the openings are generally weak in the motor case, dome-caps and wafers are used to reinforce these regions. A dome-cap is a fabric material and covers the entire dome region. A wafer is a spiral wound material and has high stiffness along the hoop direction. Wafers are 50 mm wide and cover the dome from the opening to the junction part. Dome-cap and wafers are inserted during the winding process and the location of these stiffening materials is shown in Fig. 4. Both the dome-cap and the wafer were modeled using shell elements on the faces of solid elements. It is assumed that the existence of these stiffening materials does not modify the dome geometry much. The material properties used in the analysis are shown below.

T800/epoxy for winding fibers and wafers

$E_1 = 161.3$ GPa,

$E_2 = E_3 = 8.820$ GPa,

$G_{12} = G_{13} = 5.331$ GPa,

$G_{23} = 2.744$ GPa,

$v_{12} = v_{13} = 0.33, \quad v_{23} = 0.45.$

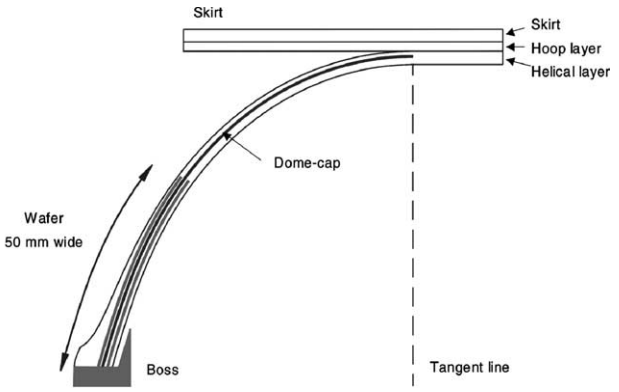

Fig. 4. The insertion location of stiffening materials.

Fabric dome-caps

$E_1 = E_2 = 67$ GPa,

$G_{12} = G_{13} = G_{23} = 12$ GPa,

$v_{12} = v_{13} = v_{23} = 0.097.$

In addition, parametric studies are done for the cases whether the wafer and the dome-cap are included or not.

Fig. 5. ASTEB configuration and specimen with strain gauges inside steel box.

3.2. Experiment

Water-pressuring tests were performed for the AS-TEB shown in Fig. 5. Because leakage or burst of the high-pressured bottle is dangerous, a steel box, 10 mm in thickness, was made for the experiments. The schematic diagram of the experimental setup is given in Fig. 6. The pressurizing device is able to push the water into the bottle up to 2000 (psi), but water-pressuring tests were done within the pressure range where the fiber breakage did not occur. The prepared composite pressure vessel in the steel box is shown in Fig. 5. 12 strain gauges, which are 2 mm in gauge length, were attached on the dome and skirt. The locations of strain gauges are shown in Fig. 7. The signals of each strain gauge and pressure transducer were measured simultaneously by an A/D converter (LabVIEW Instruments, PCI 6110E). Pressure was applied up to 913 psi (6.23 MPa) by several steps. The pressure level was held for checking the pressure drop that occurs due to leaking water at each step.

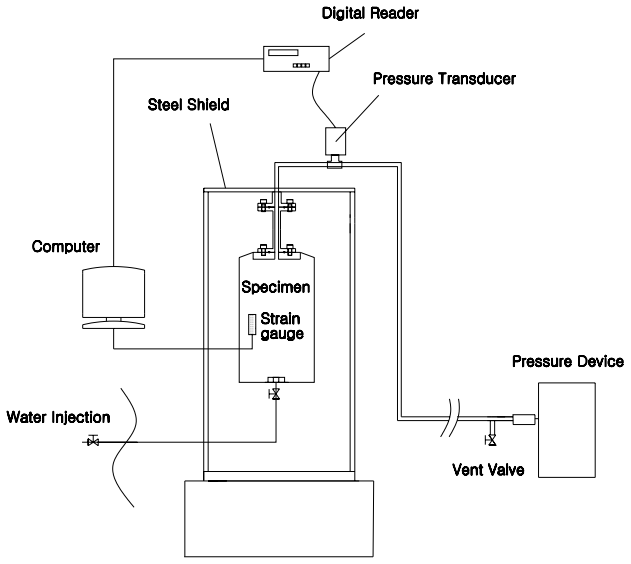

Fig. 6. Schematic diagram of experimental setup.

4. Results and discussion

4.1. Winding patterns and fiber angle change through the thickness direction

From the given dome shape of the EXOS-B, geodesic and stable winding angles are shown in Fig. 8. It is possible to wind fibers on the EXOS-B from 13.1° to 29.2° considering the frictional force between a winding tow and mandrel. When there is no slip between the fiber and mandrel ($\lambda = 0$), the fiber angle difference in the thickness direction during the winding process is about 13° at the opening of dome (Fig. 9). It is well known that major failure modes of the motor case are boss blow-outs at an undesirably low pressure. Therefore the angle variation occurring near the opening sometimes leads to a critical error in the analysis. Fig. 10 shows the angle differences for various helical winding thicknesses. As the winding thickness is getting thicker, the angle difference becomes bigger up to 16°. The fiber buildup near the opening leads to a remarkable surface change and affects the angle variation through the thickness. In

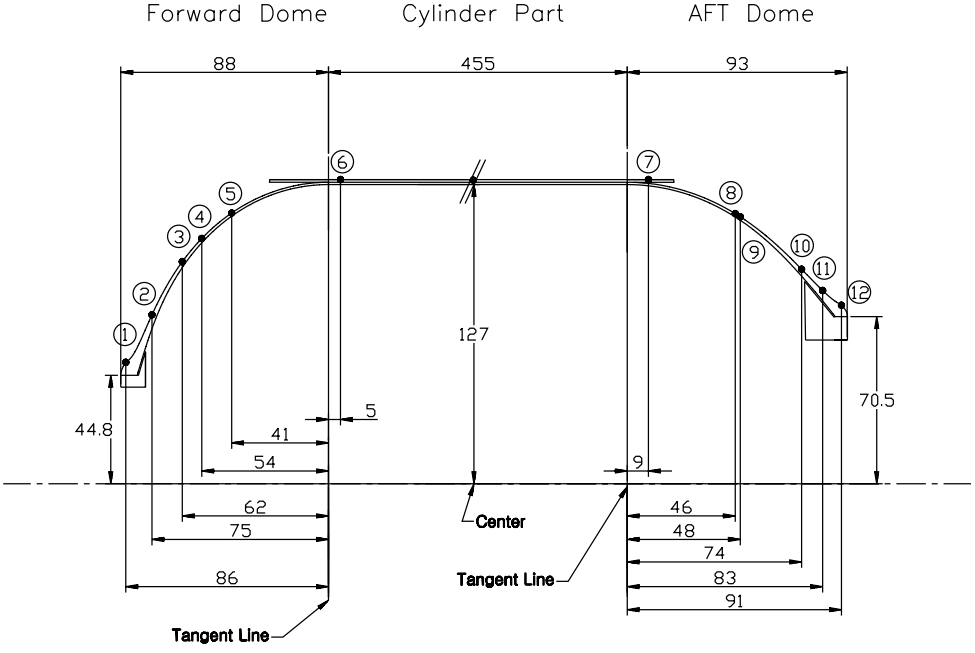

Fig. 7. Location of strain gauges attached on the bottle.

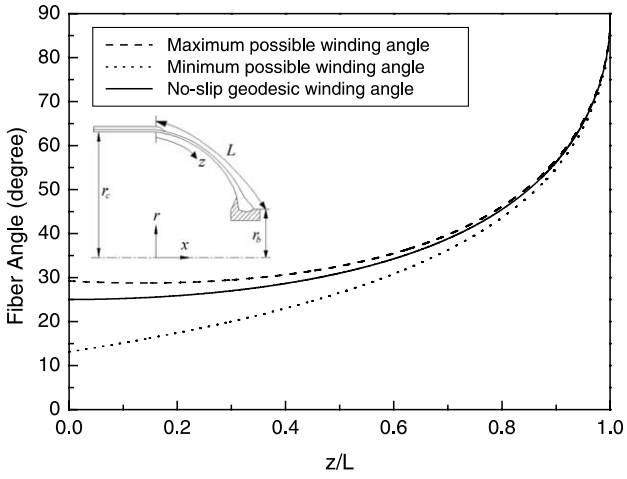

Fig. 8. Possible winding angle of EXOS-B considering fiber slip.

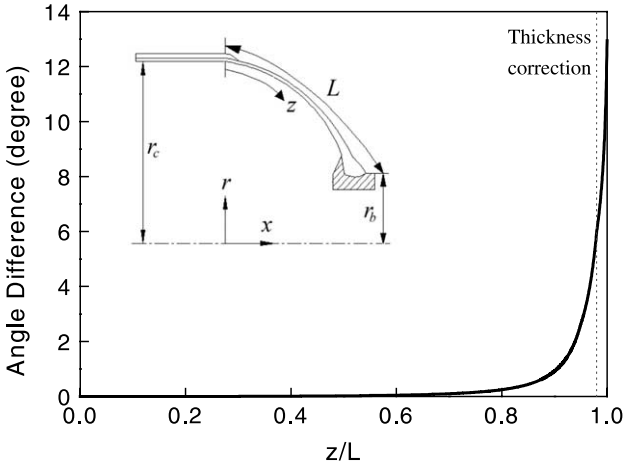

Fig. 9. Winding angle difference between first and last plies (EXOS-B).

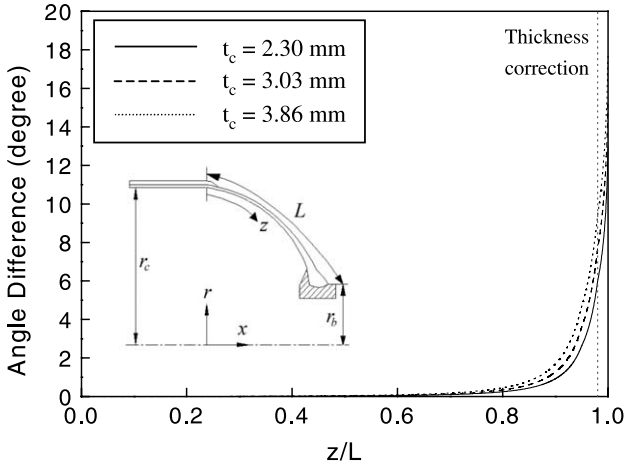

Fig. 10. Winding angle difference between first and last plies with various thicknesses of cylinder.

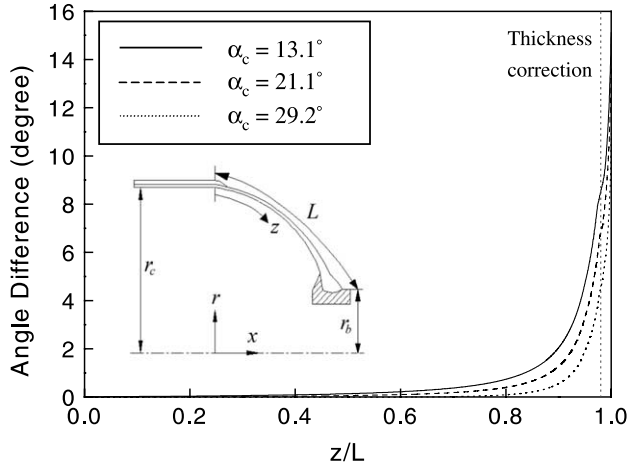

Fig. 11. Winding angle difference between first and last plies with various helical winding angles.

other words, winding angle difference through the thickness is highly affected by the winding thickness. In case of large wound structures used as a fuel, oxidizer or motor case in rockets, consideration of the winding angle change during the winding process should be required.

The effect of the winding angle on the angle difference between the first and last plies is shown in Fig. 11. Unlike helical winding thickness, various helical winding angles make totally different winding patterns and thickness distributions at the dome region. As a result, it is not possible to quantify the angle difference for each winding angle with the same thickness distribution. As the helical winding angle is getting larger, the difference in the winding angle through the thickness is getting bigger.

Therefore, the change of winding angle through the thickness should be considered when helical winding thickness and angle are reasonably large.

4.2. Finite element analysis of ASTEB and experiment

Fig. 12 shows the fiber directional strain from the experiment and the analysis. The value and tendency of the strain show good agreement with each other except the strain gauge #12. There are several reasons for the strain difference near the opening. Malfunction of a strain gauge can be a possible reason, and the boss blow-out caused from debonding between the composite and a metallic boss may induce the strain concentration near the opening. Though the strain level without serious debonding or slip between the composite and the boss is relatively low compared with the strain at the cylindrical region, burst with boss blow-outs occurs frequently unless stiffening materials such as a wafer and a dome-cap around the opening are used [9]. In other words, strain concentrations adjacent to openings are closely

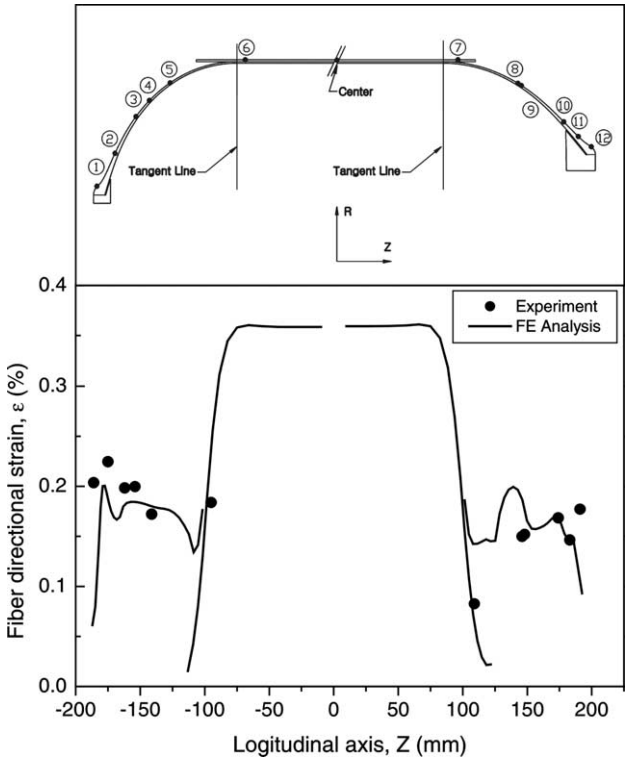

Fig. 12. Comparison of fiber directional strain between experiment and analysis (6.23 MPa).

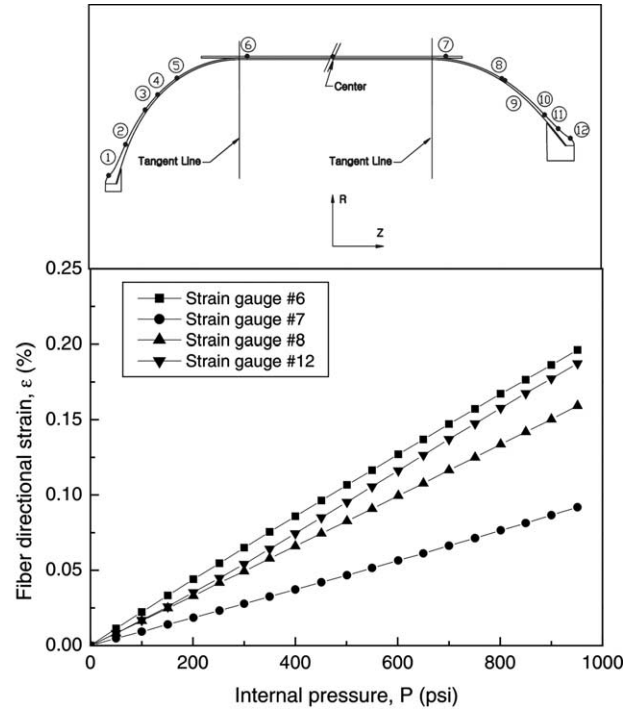

Fig. 13. Fiber directional strain vs internal pressure.

related to the failure of bonding between the composite and the metallic boss and could be analyzed precisely using progressive failure of bonding. Because the failure of materials or bonding layers is not considered in this paper, strain adjacent to the openings might be underestimated.

Fig. 13 shows the fiber directional strains vs pressure. There is no severe nonlinearity in the development of fiber directional strain. The gauge #7 is attached on the skirt, so that strain is smaller than that of gauge #6, which is located on the cylinder part.

The deformation of each dome is magnified 20 times in Figs. 14 and 15. The forward dome deformed more in the axial direction than the aft dome. Because spirally wound wafers have high stiffness along the hoop direction and relatively small stiffness in the axial direction, the effect of radial stiffening material such as a wafer is less effective in the forward dome. The fiber directional strains for various stiffening methods are shown in

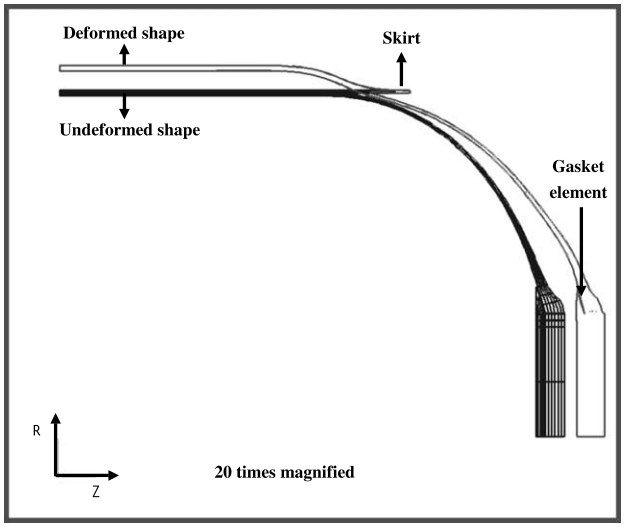

Fig. 14. Deformed shape of forward dome (20 times magnified).

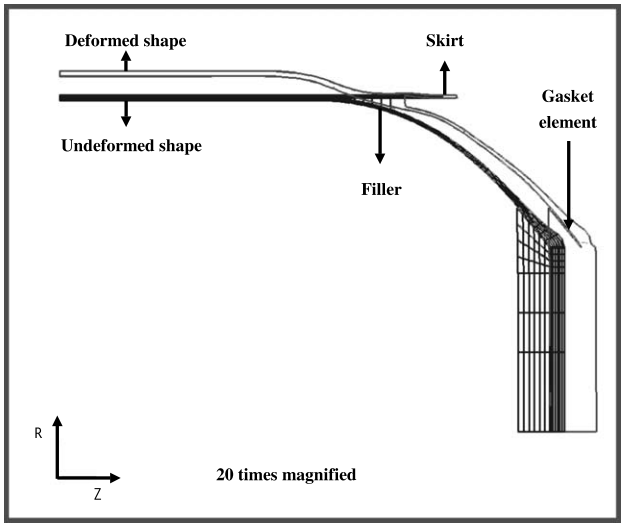

Fig. 15. Deformed shape of aft dome (20× magnified).

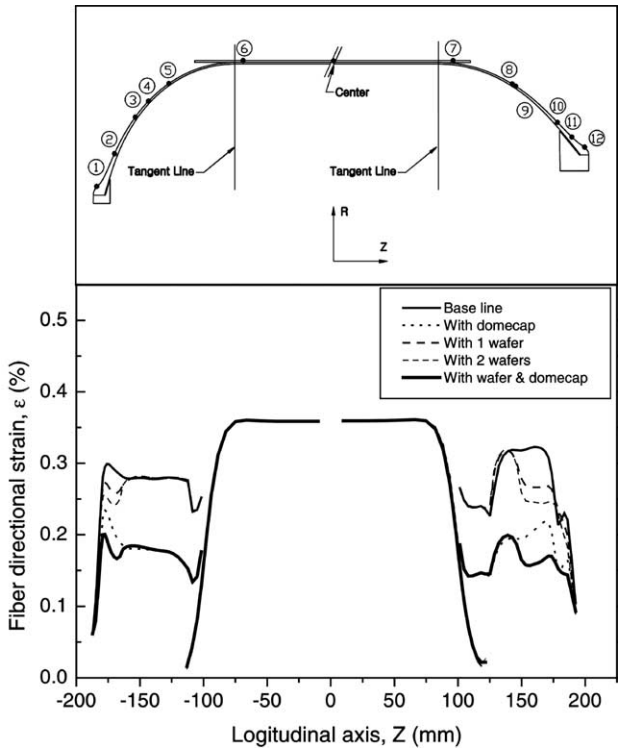

Fig. 16. Comparison of fiber directional strain with and without wafer and dome-cap (6.32 MPa).

Fig. 16. Application of the dome-cap is the most effective way to reduce the average level of strain in the dome part. Spirally wound wafers adjacent to the openings decrease the strain level in the aft dome remarkably and could prevent the metallic boss from breaking away.

5. Conclusions

The behavior of the filament wound structure subject to internal pressure was analyzed considering the winding angle change through the thickness. For several design parameters such as a helical winding angle and thickness, the amount of winding angle change in the thickness direction was quantified. The typical winding angle difference between the first and last plies reached up to 18° near the openings. In general, the boss blow-out is an important failure mode for motor cases and pressure tanks, hence it is required to consider the winding angle change through the thickness direction for the precise prediction of stress distribution over the dome and near the opening.

Water-pressuring tests were performed for the AS-TEB and the fiber directional strains measured were compared with those of the FE analysis to verify the modeling procedures. Analysis results show good agreement with experimental ones. Delicate modeling of the dome/polar opening interface made it possible to predict the stress distribution over the dome accurately. In addition, stiffening methods using the wafer and dome-cap were investigated. A dome-cap was very effective in decreasing the average level of the strain over the dome part. A wafer also could reduce the radial strain near the openings and made contributions to prevent undesirable failure in the openings.

References

[1] Uemura M. Developmental research on carbon-fiber-reinforced plastic rocket motorcase. Univ Tokyo, Report Aerospace Res Center 1979;15(4).
[2] Doh YD, Hong CS. Progressive failure analysis for filament wound pressure vessel. J Reinforced Plastics Compos 1995;14(12): 1278–306.
[3] Hartung RF. Planar-wound filamentary pressure vessels. AIAA J 1963;1:2842–4.
[4] Scholliers J, VanBrussel H. Computer-integrated filament winding: computer-integrated design, robotic filament winding and robotic quality control. Compos Manufacturing 1994;5(1):15–23.
[5] Lossie M, Van Brussel H. Design principles in filament winding. Compos Manufacturing 1994;5(1):5–13.
[6] Jeusette JP, Laschet G, Chapentier P, Deloo Ph. Finite element analysis of composite revolution structures wound by wide plies. Compos Struct 1987;8:221–37.
[7] Hwang TK, Jung SK, Doh YD, Cho WM, Jung B. The performance improvement of filament wound composite pressure vessels. In: SAMPE 2000, 2000 21–25 May. p. 1427–38.
[8] Newhouse NL, Humphrey WD. Development of the standard test and evaluation bottle (STEB). SAMPE J 1986:12–5.
[9] Newhouse NL, Humphrey WD. The standard test & evaluation bottle (STEB) five years later. SAMPE J 1986:18–23.